

The formation of a quadruple star system with wide separation

Jaime E. Pineda¹, Stella S. R. Offner^{2,3}, Richard J. Parker⁴, Héctor G. Arce⁵, Alyssa A. Goodman⁶, Paola Caselli⁷, Gary A. Fuller⁸, Tyler L. Bourke^{9,10} & Stuart A. Cordeiro^{11,12}

The initial multiplicity of stellar systems is highly uncertain. A number of mechanisms have been proposed to explain the origin of binary and multiple star systems, including core fragmentation, disk fragmentation and stellar capture^{1–3}. Observations show that protostellar and pre-main-sequence multiplicity is higher than the multiplicity found in field stars^{4–7}, which suggests that dynamical interactions occur early, splitting up multiple systems and modifying the initial stellar separations^{8,9}. Without direct, high-resolution observations of forming systems, however, it is difficult to determine the true initial multiplicity and the dominant binary formation mechanism. Here we report observations of a wide-separation (greater than 1,000 astronomical units) quadruple system composed of a young protostar and three gravitationally bound dense gas condensations. These condensations are the result of fragmentation of dense gas filaments, and each condensation is expected to form a star on a timescale of 40,000 years. We determine that the closest pair will form a bound binary, while the quadruple stellar system itself is bound but unstable on timescales of 500,000 years (comparable to the lifetime of the embedded protostellar phase¹⁰). These observations suggest that filament fragmentation on length scales of about 5,000 astronomical units offers a viable pathway to the formation of multiple systems.

Barnard 5 (B5) is a dense core in the Perseus star-forming region (at a distance of 250 pc) that hosts at least one young, forming star¹¹. Imaging of B5 in the emission of the dense-gas-tracing NH₃(1,1) line shows it to be an example of a ‘coherent’ dense core¹², which is a contiguous high-density region with subsonic levels of turbulence¹³. Higher-resolution imaging reveals narrow filamentary structure within the coherent core¹⁴. We observed the NH₃(1,1) and (2,2) lines using the Karl G. Jansky Very Large Array (VLA)¹⁵, which reveals that the filaments in B5 are fragmenting and that they are in the process of forming a wide-separation multiple stellar system.

Nearly half of all stars reside in multiple star systems^{4,16}. Consequently, a host of phenomena, ranging from supernova rates to planet formation, depend on understanding stellar multiplicity¹⁷. Because of the observational challenges associated with observing early systems, the dominant ideas for binary formation are based on simulations and analytic arguments, which naturally require a variety of assumptions^{4,18}. To date, observations have not captured the formation of a binary system at a stage where its origin is unambiguous, and prior observations of core substructure lack the spatial and kinematic resolution to be used in predicting whether observed structures would form protostars and/or produce a bound system^{19,20}. The observed kinematics and separation (>1,000 astronomical units, AU) of the B5 system is significant because it demonstrates a clear mechanism for wide binary formation and provides convincing evidence that the observed condensations will become a bound multiple star system.

Detailed knowledge of the underlying distribution of dense gas is the key to determining which structures will go on to form stars. Here we identify the dense gas structures that are most likely to form stars using the dendrogram technique²¹. Dendrogram analysis is a hierarchical structure decomposition that uses isocontours to identify individual features, while also determining where these contours merge with adjacent structures to create a new parental structure. We refer to the smallest scale (and brightest) structures in the dendrogram as condensations. These are the most likely places for an individual star to form. Figure 1a shows the B5 region as seen in dense gas (number density of H₂, $n_{\text{H}_2} \gtrsim 10^4 \text{ cm}^{-3}$), with the protostar and the identified gas condensations shown by a star and circles, respectively. The mass of the well known protostar B5-IRS1 is 0.1 solar masses (M_{Sun} ; ref. 22), while the masses of condensations B5-Cond1, B5-Cond2 and B5-Cond3 are $0.36 \pm 0.09 M_{\text{Sun}}$, $0.26 \pm 0.12 M_{\text{Sun}}$ and $0.30 \pm 0.13 M_{\text{Sun}}$, respectively. Uncertainty in these masses is dominated by the uncertainty in the temperature used to convert measured fluxes to masses. The radii of the three condensations are respectively 2,800 AU, 2,300 AU and 2,500 AU, while the projected separations between the same three condensations and the protostar are 3,300 AU, 5,100 AU and 11,400 AU (see Methods). The half-mass radii of the condensations are about half the condensation radii. This, combined with the mass radius relations (Extended Data Fig. 2), suggests that the central regions will collapse faster than the whole condensations and before interactions between condensations can play a major role in the stars’ initial separations. Although these separations are large, they are consistent with initial protostellar pair separations predicted for core fragmentation by numerical simulations². In the simulations, protostellar separations evolve rapidly on timescales of 0.1 Myr, and some systems become unbound while others migrate to closer proximity.

Projected proximity on the sky does not necessarily imply that objects are physically related. However, the line-of-sight velocities of the observed condensations are similar and the grouping is likely to be physically associated. The velocity dispersion, σ_v , of the dense gas provides another important piece of information, the gas kinetic energy, which is needed to determine whether the condensations are transient structures or gravitationally bound and likely to form a star. The velocities and velocity dispersions of the condensations are determined by fitting NH₃(1,1) and (2,2) line profiles¹⁴. The condensations and protostar display the same centroid velocity to within 0.2 km s^{-1} and are therefore associated with the same dense core. The level of turbulence in this region is so low, $\sigma_{\text{turb}} \approx 0.53\text{--}0.66$ times the sound speed in the gas¹⁴, that gravity will overwhelm the combined turbulent and thermal pressure in all the identified condensations, and a star will probably form in each case. The timescale for these condensations to undergo gravitational collapse is approximately the gas free-fall time, which we estimate to be 40,000 years (Methods). This timescale is sufficiently short to ensure that the system’s spatial

¹Institute for Astronomy, ETH Zurich, Wolfgang-Pauli-Strasse 27, CH-8093 Zurich, Switzerland. ²Department of Astronomy, Yale University, PO Box 208101, New Haven, Connecticut 06520-8101, USA. ³Department of Astronomy, University of Massachusetts, 710 North Pleasant Street, Amherst, Massachusetts 01003, USA. ⁴Astrophysics Research Institute, Liverpool John Moores University, 146 Brownlow Hill, Liverpool L3 5RF, UK. ⁵Department of Astronomy, Yale University, PO Box 208101, New Haven, Connecticut 06520-8101, USA. ⁶Harvard-Smithsonian Center for Astrophysics, 60 Garden Street, Cambridge, Massachusetts 02138, USA. ⁷Max-Planck-Institut für extraterrestrische Physik (MPE), Gießenbachstrasse 1, D-85741 Garching, Germany. ⁸UK ARC Node, Jodrell Bank Centre for Astrophysics, School of Physics and Astronomy, Alan Turing Building, Oxford Road, University of Manchester, Manchester M13 9PL, UK. ⁹SKA Organisation, Jodrell Bank Observatory, Lower Withington, Macclesfield, Cheshire SK11 9DL, UK. ¹⁰Harvard-Smithsonian Center for Astrophysics, 60 Garden Street, Cambridge, Massachusetts 02138, USA. ¹¹Joint ALMA Observatory, Alonso de Cordova 3107, Vitacura, Santiago, Chile. ¹²National Radio Astronomy Observatory, 520 Edgemont Road, Charlottesville, Virginia 22903, USA.

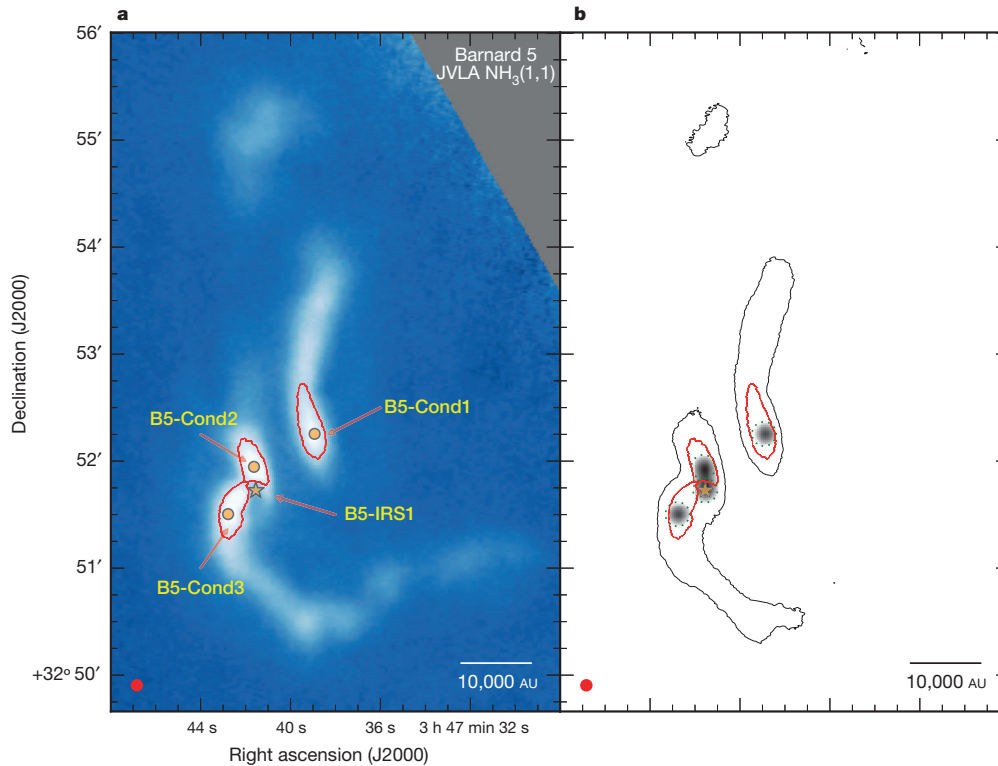


Figure 1 | High-angular-resolution image of dense gas and stellar progenitors. **a**, Background image from the JVLA of the Barnard 5 region shows the dense gas traced by $\text{NH}_3(1,1)$. It reveals two filaments, which together host three gravitationally bound condensations (B5-Cond1, 2, 3). Red contours and orange-filled circles show the condensation boundaries and centres, while the star indicates the protostar (B5-IRS1) location. **b**, Contour map showing the filaments in dense gas. Greyscale circles show the distance that could be covered during 40,000 years while moving at the speed of sound, 0.2 km s^{-1} . In **a** and **b**, filled red circle at bottom left shows the angular resolution of the observations, and scale bar is shown at bottom right.

configuration will remain nearly unchanged during collapse, even if the protostars move as far as possible (in straight lines at the gas sound speed) for the duration of the collapse ($<1,700 \text{ AU}$ or $6.8''$ at the distance of Perseus). Figure 1b shows, as dotted circles, the possible ranges over which protostars could move in a free-fall time. The circles are smaller than the current condensation radii, so we conclude that this is a multiple system caught at the beginning of its formation.

In order to determine if the multiple stellar system is bound, it is necessary to estimate the masses of the stars that will be formed within the condensations. However, there are two complicating factors that make mass estimates uncertain. First, we must estimate what fraction of the condensation mass will end up in the star. Comparison between the initial mass function of stars and the distribution of dense core masses suggests that individual cores have a star formation efficiency of $\epsilon_{\text{DenseCore}} = M_{\text{Star}}/M_{\text{DenseCore}} \approx 30\%$ (refs 23–25). Theoretical estimates based on the effects of protostellar outflows predict core efficiencies of $\epsilon_{\text{DenseCore}} = 25\text{--}75\%$ (refs 26–28). Here, the condensations are embedded inside a previously identified dense core, B5, and they have radii one-tenth those of typical dense cores. Therefore, it would not be surprising if their star formation efficiency is close to 100%, at $\epsilon_{\text{Condensation}} = M_{\text{Star}}/M_{\text{Condensation}} \approx 75\%$ (ref. 26). Second, since the condensations are embedded within dense filaments, it is possible that the final stellar masses will be higher than the current measured condensation mass, because additional gas can flow along the filaments and accrete onto the condensations^{29,30}. If we adopt a very conservative estimate for the efficiency of 30%, and assume no additional mass accretion from the filaments, the final stellar masses formed from the condensations will be above the brown dwarf limit (80 Jupiter masses). Further fragmentation could occur within the condensations, however, given the low multiplicity fraction at these masses, $<26\%$ (ref. 4), so for our analysis we assume the most likely outcome, single stars. The lower the final stellar masses, the less likely the system is to be bound, so we

have made the most pessimistic assumptions possible (giving the lowest stellar masses) in evaluating boundedness.

Depending on the final stellar masses and kinematics, the resulting multiple stellar system could either be strongly bound or quickly dissolve owing to dynamical interactions. Given the dynamical instability of higher order systems, it is very likely that even if all the stars are initially bound, one or more will be dynamically ejected at a later time^{8,9}. For the closest possible pair, B5-IRS1 and B5-Cond2, we calculate the energies for a wide range of final stellar masses and under different kinematical and spatial distribution assumptions. In each case, we make different assumptions to reconstruct the total velocity dispersion and total separation based on our measured line-of-sight values. Figure 2 shows that the ratio of kinetic to gravitational energy is much less than one for all these cases, and therefore the pair is gravitationally bound.

Similarly, we compare the kinetic and gravitational energies for the expected stellar system taken all together, and find that the quadruple system is bound. Although bound, it is not likely to be a stable hierarchical system in the long term (see Methods), and the system will probably dissipate into a wide-separation binary system (B5-IRS1 and B5-Cond2). An important caveat is that this analysis does not take into account the effect of gas. The system is embedded in a larger reservoir of gas (the B5 core), which is several times the combined mass of the condensations. This additional gas can have two effects on the system evolution. First, the gravitational potential of the dense gas enhances the binding energy of the system by increasing the stellar escape velocity. Eventually, much of this gas will be removed by outflows. Second, the gas acts as a drag force on the stars, dissipating some of the stellar kinetic energy. Both these effects support the same outcome: a bound stellar system, at least during the formation stage. These results show that fragmentation of filaments would happen at scales smaller than those predicted by Jeans fragmentation of dense cores^{14,25}, and therefore filaments (or substructure in general) might be crucial ingredients in the formation of multiples.

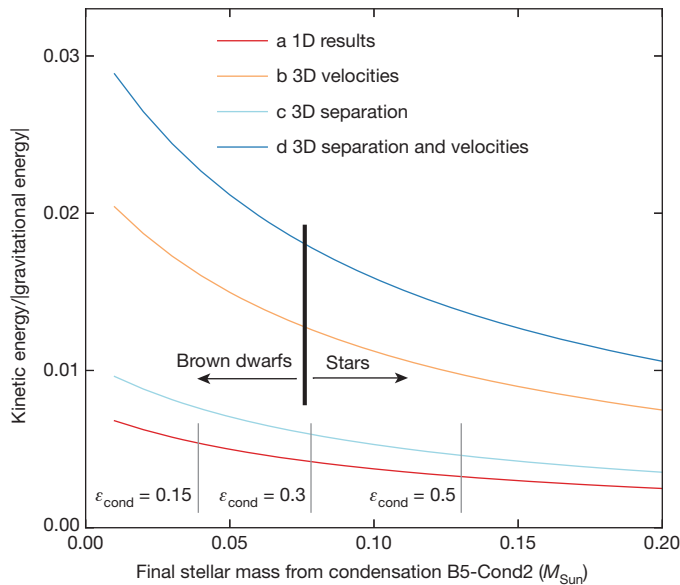


Figure 2 | Ratio of kinetic to gravitational energy for B5-IRS1 and B5-Cond2 as a function of final stellar mass. A binary system is bound if the kinetic-to-gravitational energy ratio is below unity. We calculate the energies for a wide range of efficiencies, $\epsilon_{\text{Condensation}} = M_{\text{Star}}/M_{\text{Condensation}}$, and under different kinematical and spatial distribution assumptions (see text for details) for the B5-IRS1 protostar and the final object from condensation B5-Cond2. First, we use the on-sky separation and the line-of-sight velocity difference as the total binary distance and velocity difference (line a, red). Next, we assume that the velocity difference along the line-of-sight is representative for the difference in the other directions, and therefore the total velocity difference is $\sqrt{3}$ times the velocity difference along the line-of-sight (line b, orange). Line c (light blue) assumes that the binary separation on the plane of the sky is a good estimate for the separation along the line-of-sight, and therefore the total separation is estimated as $\sqrt{2}$ times the separation on the plane of the sky. Finally, we compute the energies assuming both b and c together (line d, dark blue). Grey vertical lines denote some representative efficiencies, $\epsilon_{\text{Condensation}}$. Black vertical line marks the upper mass limit for a brown dwarf ($0.076M_{\text{Sun}}$). This figure shows that for all estimates the closest separation binary is bound.

Additional observations of the distribution of dense gas in other regions using the VLA and/or Atacama Large Millimeter Array (ALMA) will determine the frequency of occurrence of filaments (or substructure) in dense cores and the distribution of separations of pre-stellar condensations at birth.

Online Content Methods, along with any additional Extended Data display items and Source Data, are available in the online version of the paper; references unique to these sections appear only in the online paper.

Received 18 September; accepted 24 December 2014.

- Stamatellos, D. & Whitworth, A. P. The properties of brown dwarfs and low-mass hydrogen-burning stars formed by disc fragmentation. *Mon. Not. R. Astron. Soc.* **392**, 413–427 (2009).
- Offner, S. S. R., Kratter, K. M., Matzner, C. D., Krumholz, M. R. & Klein, R. I. The formation of low-mass binary star systems via turbulent fragmentation. *Astrophys. J.* **725**, 1485–1494 (2010).
- Moekel, N. & Bate, M. R. On the evolution of a star cluster and its multiple stellar systems following gas dispersal. *Mon. Not. R. Astron. Soc.* **404**, 721–737 (2010).
- Duchêne, G. & Kraus, A. Stellar multiplicity. *Annu. Rev. Astron. Astrophys.* **51**, 269–310 (2013).
- Chen, X. *et al.* SMA observations of class 0 protostars: a high angular resolution survey of protostellar binary systems. *Astrophys. J.* **768**, 110 (2013).
- Connelley, M. S., Reipurth, B. & Tokunaga, A. T. The evolution of the multiplicity of embedded protostars. I. Sample properties and binary detections. *Astron. J.* **135**, 2496–2525 (2008).

- Connelley, M. S., Reipurth, B. & Tokunaga, A. T. The evolution of the multiplicity of embedded protostars. II. Binary separation distribution and analysis. *Astron. J.* **135**, 2526–2536 (2008).
- Reipurth, B. & Mikkola, S. Formation of the widest binary stars from dynamical unfolding of triple systems. *Nature* **492**, 221–224 (2012).
- Reipurth, B. *et al.* Multiplicity in early stellar evolution. Preprint at <http://arXiv.org/abs/1403.1907> (2014).
- Evans, N. J., II *et al.* The Spitzer c2d legacy results: star-formation rates and efficiencies; evolution and lifetimes. *Astrophys. J.* **181**, 321–350 (2009).
- Fuller, G. A. *et al.* Anatomy of the Barnard 5 core. *Astrophys. J.* **376**, 135–149 (1991).
- Pineda, J. E. *et al.* Direct observation of a sharp transition to coherence in dense cores. *Astrophys. J.* **712**, L116–L121 (2010).
- Goodman, A. A., Barranco, J. A., Wilner, D. J. & Heyer, M. H. Coherence in dense cores. II. The transition to coherence. *Astrophys. J.* **504**, 223–246 (1998).
- Pineda, J. E. *et al.* Expanded Very Large Array observations of the Barnard 5 star-forming core: embedded filaments revealed. *Astrophys. J.* **739**, L2 (2011).
- Perley, R. A., Chandler, C. J., Butler, B. J. & Wrobel, J. M. The expanded Very Large Array: a new telescope for new science. *Astrophys. J.* **739**, L1 (2011).
- Lada, C. J. Stellar multiplicity and the initial mass function: most stars are single. *Astrophys. J.* **640**, L63–L66 (2006).
- Parker, R. J. & Quanz, S. P. On the frequency of planetary systems around G dwarfs. *Mon. Not. R. Astron. Soc.* **436**, 650–658 (2013).
- Tohline, J. E. The origin of binary stars. *Annu. Rev. Astron. Astrophys.* **40**, 349–385 (2002).
- Kamazaki, T., Saito, M., Hirano, N. & Kawabe, R. Millimeter-wave interferometric study of the rho Ophiuchi A region. I. Small-scale structures of dust continuum sources. *Astrophys. J.* **548**, 278–287 (2001).
- Nakamura, F., Takakuwa, S. & Kawabe, R. Substellar-mass condensations in prestellar cores. *Astrophys. J.* **758**, L25 (2012).
- Rosolowsky, E. W., Pineda, J. E., Kauffmann, J. & Goodman, A. A. Structural analysis of molecular clouds: dendrograms. *Astrophys. J.* **679**, 1338–1351 (2008).
- Brassfield, E. & Bourke, T. L. Submillimeter Array observations of embedded class I object Barnard 5 IRS1. *Bull. Am. Astron. Soc.* **43**, 340.09 (2011).
- Motte, F., Andre, P. & Neri, R. The initial conditions of star formation in the rho Ophiuchi main cloud: wide-field millimeter continuum mapping. *Astron. Astrophys.* **336**, 150–172 (1998).
- Alves, J., Lombardi, M. & Lada, C. J. The mass function of dense molecular cores and the origin of the IMF. *Astron. Astrophys.* **462**, L17–L21 (2007).
- André, P. *et al.* From filamentary networks to dense cores in molecular clouds: toward a new paradigm for star formation. Preprint at <http://arXiv.org/abs/1312.6232> (2014).
- Matzner, C. D. & McKee, C. F. Efficiencies of low-mass star and star cluster formation. *Astrophys. J.* **545**, 364–378 (2000).
- Machida, M. N. & Hosokawa, T. Evolution of protostellar outflow around low-mass protostar. *Mon. Not. R. Astron. Soc.* **431**, 1719–1744 (2013).
- Offner, S. S. R. & Arce, H. G. Investigations of protostellar outflow launching and gas entrainment: hydrodynamic simulations and molecular emission. *Astrophys. J.* **784**, 61 (2014).
- Kirk, H. *et al.* Filamentary accretion flows in the embedded Serpens South protocluster. *Astrophys. J.* **766**, 115 (2013).
- Peretto, N. *et al.* Global collapse of molecular clouds as a formation mechanism for the most massive stars. *Astron. Astrophys.* **555**, A112 (2013).

Acknowledgements We thank K. Todorov for discussions and comments that improved the paper. We acknowledge support from the Swiss National Science Foundation project CRSII2_141880 (J.E.P.), NSF CAREER award AST-0845619 (H.G.A.), NSF grant AST-0908159 (A.A.G.), ERC project PALs 320620 (P.C.) and NASA grant NNX09AB89G (T.L.B.). S.S.R.O. acknowledges support from NASA through Hubble Fellowship grant 51311.01 awarded by the Space Telescope Science Institute, which is operated by the Association of Universities for Research in Astronomy, Inc., for NASA, under contract NAS 5-26555. R.J.P. acknowledges support from the Royal Astronomical Society through a research fellowship. This research made use of *astrodendro* (<http://www.dendrograms.org>), *Astropy*, and *APLpy* (<http://aplpy.github.com>). The James Clerk Maxwell Telescope is operated by the Joint Astronomy Centre on behalf of the Science and Technology Facilities Council of the UK, the National Research Council of Canada, and (up to 31 March 2013) the Netherlands Organisation for Scientific Research. Additional funds for the construction of SCUBA-2 were provided by the Canada Foundation for Innovation. The National Radio Astronomy Observatory is a facility of the NSF operated under cooperative agreement by Associated Universities, Inc.

Author Contributions J.E.P. led the project and reduced the VLA data. J.E.P. and S.S.R.O. wrote the manuscript. R.J.P. conducted the stability analysis of the multiple system. All authors contributed to the VLA proposal, discussed the results and implications, and commented on the manuscript.

Author Information Reprints and permissions information is available at www.nature.com/reprints. The authors declare no competing financial interests. Readers are welcome to comment on the online version of the paper. Correspondence and requests for materials should be addressed to J.E.P. (jpineda@mpe.mpg.de).

METHODS

Observations and data reduction. *Very Large Array.* We conducted VLA observations of the B5 region on 2011 October 16–17 in D-array configuration, and on 2012 January 13–14 in CnD-array configuration (project 11B-101). We used the high-frequency K-band receiver and configured the WIDAR correlator to observe two basebands of 4 MHz bandwidth around the $\text{NH}_3(1,1)$ and $(2,2)$ lines. Each baseband is split into 8 adjacent spectral windows of 500 kHz bandwidth, with a channel separation of 0.049 km s^{-1} . The quasar 3C 48 was used as flux calibrator, 3C 84 as the bandpass calibrator, and J0336+3218 as the phase calibrator.

We reduced the data with the Common Astronomy Software Applications package³¹. The images were created using multi-scale clean (with scales of 0, 4 and 12 arcsec and `smallscalebias` parameter of 0.2) with a robust parameter of 0.5 and a 6 arcsec beam. We also included the NH_3 single dish data obtained with the Robert C. Byrd Green Bank Telescope³² as a model image to recover the extended emission. The image has a noise level of 4 mJy per beam per channel.

The integrated emission map is calculated using all hyperfine components in the following velocity range: $(-10.016, -8.534) \text{ km s}^{-1}$, $(1.845, 3.575) \text{ km s}^{-1}$, $(9.012, 11.483) \text{ km s}^{-1}$, $(9.012, 11.483) \text{ km s}^{-1}$, $(16.919, 18.896) \text{ km s}^{-1}$, and $(28.781, 30.758) \text{ km s}^{-1}$. The final noise achieved is $2.8 \text{ mJy per beam km s}^{-1}$.

James Clerk Maxwell Telescope (JCMT). We observed B5 in the dust continuum emission at $450 \mu\text{m}$ and $850 \mu\text{m}$ using the Submillimetre Common-User Bolometer Array 2 (SCUBA-2) bolometer array³² at the JCMT. The observations were carried out on 2013 August 16 and 23, and on 2013 August 3 under project M13BU14 during grade 1 weather. We use the iterative map-making technique, `makemap`³³, with 0.5 arcsec pixels to match the $\text{NH}_3(1,1)$ VLA map. The initial reductions of the scans are co-added to create a mosaic, which we use to create a mask of signal-to-noise ratio >5 . Our final mosaic is created by co-adding a second reduction of the individual scans where the mask defines areas with emission. The angular resolution at $450 \mu\text{m}$ and $850 \mu\text{m}$ is 9.8 arcsec and 14.6 arcsec (ref. 34), respectively. We only use the $450 \mu\text{m}$ map, since its resolution is similar to the VLA observations.

We calibrate the flux scale of the observations using the Flux Correction Factor (FCF) of $4.71 \pm 0.5 \text{ Jy pW}^{-1} \text{ arcsec}^{-2}$ for $450 \mu\text{m}$ and of $2.34 \pm 0.08 \text{ Jy pW}^{-1} \text{ arcsec}^{-2}$ for $850 \mu\text{m}$ (ref. 34). We measure a noise level of $0.026 \text{ mJy per pixel}$ and $0.23 \text{ mJy per pixel}$ in the emission-free regions of the $850 \mu\text{m}$ and $450 \mu\text{m}$ maps. Extended Data Fig. 1 shows the final SCUBA-2 $450 \mu\text{m}$ and $850 \mu\text{m}$ maps, in which both the condensation B5-Cond1 and bright emission around the protostar B5-IRS1 are clearly detected, while condensations B5-Cond2 and B5-Cond3, although detected, are overwhelmed by the emission from B5-IRS1. The morphology of the emission is similar to the $\text{NH}_3(1,1)$ emission map, confirming the filamentary structure and the condensations.

Condensation identification. We use the dendrogram algorithm²¹ to identify the structures in the $\text{NH}_3(1,1)$ integrated intensity map. Each structure corresponds to a surface of constant intensity. An advantage of the algorithm is that structures can be nested inside one another, representing the hierarchy of the cloud, and then simply visualized using a tree diagram. The condensations are the ‘leaves’, that is, the highest level in the dendrogram decomposition. We produce the dendrogram with the following parameters: `min_value` = $4\sigma_{\text{rms}}$ (minimum intensity considered in the analysis), `min_delta` = $2\sigma_{\text{rms}}$ (minimum spacing between isocontours), and `min_npix` = 250 (minimum number of pixels contained in a structure), where $\sigma_{\text{rms}} = 5 \text{ mJy per beam km s}^{-1}$ is the rms noise. The condensation radius, R_{eq} , is defined as the equivalent radius, $\pi R_{\text{eq}}^2 = \text{area}$.

The centroid velocity of each condensation is computed by averaging the centroid velocity within a $6 \text{ arcsec} \times 6 \text{ arcsec}$ box centred at the peak emission in the $\text{NH}_3(1,1)$ map. The velocity dispersion of each condensation is determined by taking the average of the velocity dispersions within the condensation. In both cases, the uncertainties are estimated from the standard deviation of the quantities measured.

The total flux for each condensation is defined as the total flux minus the background emission removed within the structure boundary determined by the dendrogram. Extended Data Table 1 displays the fluxes calculated from the $\text{NH}_3(1,1)$ emission map for all condensations. Of the three condensations, only B5-Cond1 flux is not contaminated by the bright B5-IRS1 in the SCUBA-2 $450 \mu\text{m}$ dust emission continuum, and we include its total flux in the table.

Mass determination for condensations. We determine the total mass of B5-Cond1 using the total flux of the SCUBA-2 $450 \mu\text{m}$ dust emission map assuming optically thin emission,

$$M_{\text{dust}} = d^2 F_{\nu} / (\kappa_{\nu} B_{\nu}(T))$$

where d is the distance, F_{ν} is the total flux, κ_{ν} is the dust opacity per unit mass at frequency ν , and $B_{\nu}(T)$ is the Planck function at temperature T . We use a dust to gas ratio of 0.01, and a dust opacity per unit mass of $\kappa_{\nu} = 0.1(\nu/1 \text{ THz})^2$ (ref. 35), which at $450 \mu\text{m}$ gives $\kappa_{450\mu\text{m}} = 0.044 \text{ cm}^2 \text{ g}^{-1}$. We assume a temperature of $T = 10 \text{ K}$,

which is the typical temperature of starless cores in Perseus³⁶, and distance of 250 pc (ref. 37). In the case of B5-Cond1, this gives a mass estimate of $0.39 M_{\text{Sun}}$.

We use the mass-to- NH_3 flux ratio derived from B5-Cond1, whose isolation makes mass calculations most reliable, to estimate the masses of condensations B5-Cond2 and B5-Cond3. This gives masses of $0.33 M_{\text{Sun}}$ and $0.39 M_{\text{Sun}}$ for B5-Cond2 and B5-Cond3, respectively.

We also plot the enclosed mass as a function of radius in Extended Data Fig. 2a. Here we also compare these mass–radius relations with those predicted for density profile of $\rho \propto r^{-2}$ and $\rho \propto r^{-1.5}$, and it is clear that the condensations are better described by a $\rho \propto r^{-1.5}$ density profile between 800 AU and 1,900 AU. A density profile of $\rho \propto r^{-2}$ is a good description for a core in (or close to) hydrostatic equilibrium, while a profile of $\rho \propto r^{-1.5}$ is a good model for free falling envelopes³⁸. This also supports the notion that the condensations in B5 are centrally concentrated and close to forming a central object.

Virial analysis for condensations. We calculate the virial parameter (the ratio between kinetic and gravitational energy) for a spherical core assuming a density profile $\rho \propto r^{-1.5}$ (ref. 39), which (see above) is a good approximation for the condensation’s density profile from 800 AU to 1,900 AU (see Extended Data Fig. 2):

$$\alpha = 4 R \sigma_v^2 / G M = 928(R/\text{pc})(M/M_{\text{Sun}})^{-1}(\sigma_v/\text{km s}^{-1})^2$$

where R is the radius, M is the mass, and σ_v is the total velocity dispersion of the gas (including thermal and non-thermal components, $\sigma_v^2 = \sigma_{\text{th}}^2 + \sigma_{\text{turb}}^2$). A condensation is bound if $\alpha < 2$.

The average level of turbulence, σ_{turb} , measured towards condensations B5-Cond1, B5-Cond2 and B5-Cond3 is $0.66 \times \sigma_{\text{th}}$, $0.58 \times \sigma_{\text{th}}$ and $0.54 \times \sigma_{\text{th}}$, respectively, where $\sigma_{\text{th}} = 0.2 \text{ km s}^{-1}$ is the sound speed of the gas with mean molecular weight per free particle for $\mu = 2.33$ and at a temperature of 10 K.

We calculate the virial parameter as a function of radius for each condensation using its measured average velocity dispersion (Extended Data Fig. 2b); the condensations are all bound beyond a radius of 1,200 AU. The virial parameter initially decreases as a function of radius until it reaches a minimum at $\sim 60\%$ of the condensation radius, and then it increases until it reaches the edge of the condensation as defined by the dendrogram, while staying bound (Extended Data Fig. 2b).

Free-fall timescale. The free-fall timescale for a uniform density sphere is defined as

$$t_{\text{ff}} = \sqrt{\frac{3\pi}{32G\rho}} = \sqrt{\frac{\pi^2 R^3}{8GM}} = 1.6 \times 10^6 \left(\frac{R}{0.1 \text{ pc}}\right)^{3/2} \left(\frac{M}{0.1 M_{\text{Sun}}}\right)^{-1/2} \text{ yr}$$

where $M = 4\pi R^3 \rho / 3$. The free-fall timescale, t_{ff} , is $4.0 \times 10^4 \text{ yr}$, $3.5 \times 10^4 \text{ yr}$, and $4.1 \times 10^4 \text{ yr}$ for B5-Cond1, B5-Cond2 and B5-Cond3, respectively. Thus, about 40,000 years is the ‘typical’ free-fall timescale for this system. This definition excludes the influence of magnetic fields, which could delay collapse.

Stability analysis of the multiple system. We calculate the potential and kinetic energy of each object and determine if all of the objects are bound⁴⁰. The gravitational potential energy, V_{ij} , is calculated as

$$V_i = - \sum_{j \neq i} \frac{G m_i m_j}{r_{ij}}$$

where m_i and m_j are the masses of objects i and j , and r_{ij} is the distance between them. The kinetic energy of each object, T_i , is given by

$$T_i = \frac{1}{2} m_i (v_i - v_{\text{com}})^2$$

where v_i is the (line-of-sight) velocity of object i , and v_{com} is the velocity of the centre of mass of the system. A star is bound to the system if $T_i/|V_i| < 1$.

Using the stellar mass estimates, two-dimensional positions, and one-dimensional line-of-sight velocities, we find that all four objects comprise a bound system. The calculated kinetic-to-gravitational energy ratio of the system is 0.11. In order to assess the robustness of this result, we remove each object in turn from the analysis and find that the system remains bound. If we were to increase the mass of any of the four objects, this would decrease the energy ratio further.

We next determine whether any of the four objects will become a stable binary or triple system, with the caveat that we only know the velocity along the line-of-sight and the separation on the sky. We determine the binding energy, semimajor axis, and eccentricity of the central or ‘inner’ system (B5-IRS1 + B5-Cond2). We determine the eccentricity using the following formula⁴¹:

$$e = \sqrt{\left(1 + \frac{2(m_1 + m_2)L_{\text{tot}}^2 E_{\text{bind}}}{G^2 m_1^3 m_2^3}\right)}$$

where m_1 and m_2 are the component masses, L_{tot} is the magnitude of the total angular momentum vector on the centre of mass frame, and E_{bind} is the binding energy.

The angular momentum is calculated using only the line-of-sight velocity and the projected on-sky separation between the considered components, $L_{\text{tot}} = [m_1 m_2 / (m_1 + m_2)] [(x_2 - x_1, y_2 - y_1, 0) \times (0, 0, v_2 - v_1)]$, where x_i and y_i are the on-sky relative positions and v_i are the line-of-sight velocities. The binding energy is negative, and the semimajor axis is $a_{\text{in}} = 1,666$ AU with a high eccentricity of 0.99. We note that changing the component masses has a minimal effect on the semimajor axis and eccentricity values (if all the masses are $0.2 M_{\text{Sun}}$, then $a_{\text{in}} = 1,663$ AU, $e_{\text{in}} = 0.99$ and the system remains bound). However, the determination of a high eccentricity must be taken with caution, because its uncertainty is mostly due to the lack of knowledge about the full orbital elements.

Next, we treat the central system as the inner orbit of a triple system and determine whether either [(B5-IRS1 + B5-Cond2) + B5-Cond3] or [(B5-IRS1 + B5-Cond2) + B5-Cond1] could be a stable triple system. The former system could be a stable triple because it has a negative binding energy; the outer semimajor axis of this system is $a_{\text{out}} = 4,060$ AU, the eccentricity is 0.50, and the inner and outer orbit periods are 2×10^5 yr and 5×10^5 yr, respectively.

However, we note that as the on-sky separation of the inner system (B5-IRS1 + B5-Cond2) is less than 5–10 times the separation of the outer system [(B5-IRS1 + B5-Cond2) + B5-Cond3], which makes it highly likely to be unstable over long timescales⁸.

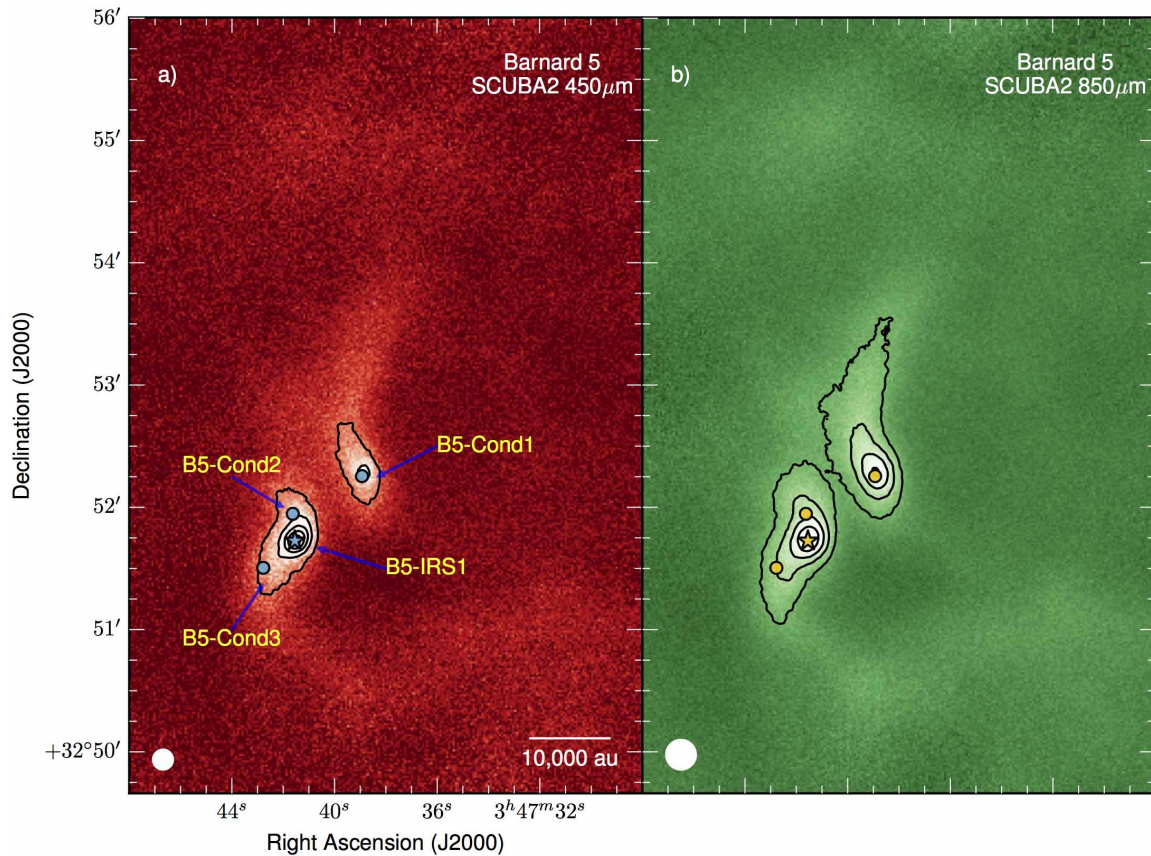
Finally, we find that the [(B5-IRS1 + B5-Cond2) + B5-Cond1] system has a positive binding energy, and is therefore not a stable bound system.

In summary, the four objects together are bound, but they do not constitute a stable hierarchical quadruple system. The central (B5-IRS1 + B5-Cond2) system is a bound binary (albeit with high eccentricity) and may make up a triple system with [(B5-IRS1 + B5-Cond2) + B5-Cond3].

The fate of this system will probably be determined by internal evolution, that is, whether or not it becomes unstable, rather than by external perturbations⁴¹, owing to it forming in a low stellar density environment.

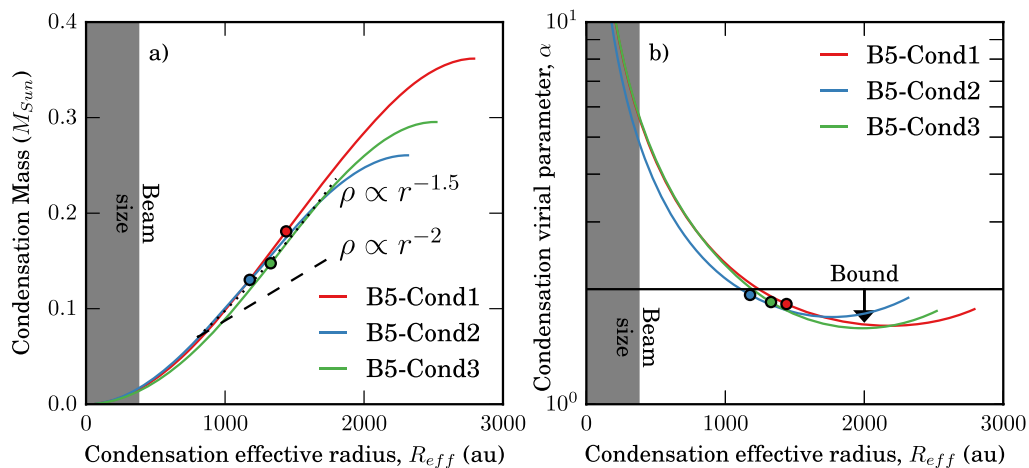
Code availability. The code used in this research is freely available at https://github.com/jpinedaf/B5_wide_multiple, it makes use of Astropy⁴².

31. McMullin, J. P., Waters, B., Schiebel, D., Young, W. & Golap, K. in *Astronomical Data Analysis Software and Systems XVI* (eds Shaw, R. A., Hill, F. & Bell, D. J.) 127–130 (Astron. Soc. Pacif. Conf. Ser. Vol. 376, 2007).
32. Holland, W. S. *et al.* SCUBA-2: the 10,000 pixel bolometer camera on the James Clerk Maxwell Telescope. *Mon. Not. R. Astron. Soc.* **430**, 2513–2533 (2013).
33. Chapin, E. L. *et al.* SCUBA-2: iterative map-making with the Sub-Millimetre User Reduction Facility. *Mon. Not. R. Astron. Soc.* **430**, 2545–2573 (2013).
34. Dempsey, J. T. *et al.* SCUBA-2: on-sky calibration using submillimetre standard sources. *Mon. Not. R. Astron. Soc.* **430**, 2534–2544 (2013).
35. Hildebrand, R. H. The determination of cloud masses and dust characteristics from submillimetre thermal emission. *Q. J. R. Astron. Soc.* **24**, 267–282 (1983).
36. Foster, J. B. *et al.* Dense cores in Perseus: the influence of stellar content and cluster environment. *Astrophys. J.* **696**, 298–319 (2009).
37. Enoch, M. L. *et al.* Bolocam survey for 1.1 mm dust continuum emission in the c2d legacy clouds. I. Perseus. *Astrophys. J.* **638**, 293–313 (2006).
38. Shu, F. H. Self-similar collapse of isothermal spheres and star formation. *Astrophys. J.* **214**, 488–497 (1977).
39. Enoch, M. L. *et al.* The mass distribution and lifetime of prestellar cores in Perseus, Serpens, and Ophiuchus. *Astrophys. J.* **684**, 1240–1259 (2008).
40. Baumgardt, H., Hut, P. & Heggie, D. C. Long-term evolution of isolated N-body systems. *Annu. Rev. Astron. Astrophys.* **336**, 1069–1081 (2002).
41. Parker, R. J. & Meyer, M. R. Binaries in the field: fossils of the star formation process? *Mon. Not. R. Astron. Soc.* **442**, 3722–3736 (2014).
42. Astropy Collaboration *et al.* Astropy: A community Python package for astronomy. *Astron. Astrophys.* **558**, A33 (2013).



Extended Data Figure 1 | Dust continuum emission maps of Barnard 5.
a, b, Dust continuum emission observed with SCUBA-2 at 450 μm (**a**) and 850 μm (**b**). Contour levels are drawn at 3, 6, 9, 12 and 15× rms, where rms is 0.23 mJy per pixel and 0.026 mJy per pixel in the 450 μm and 850 μm maps, respectively. Emission from dust associated with the protostar B5-IRS1 dominates the field, and it makes it difficult to extract the emission from

B5-Cond2 and B5-Cond3. B5-Cond1 is clearly detected in the dust continuum emission. Since the dust continuum emission does show the presence of the filaments in low level emission, we conclude they are real column density features. Filled white circles at bottom left corners show the angular resolution of the observations. Blue- and orange-filled circles show the condensation centres, while the filled stars indicate the protostar (B5-IRS1) location.



Extended Data Figure 2 | Mass and virial parameter as a function of radius for condensations. **a**, The enclosed condensation mass, derived from $\text{NH}_3(1,1)$, at different effective radii for each condensation; **b**, the corresponding virial parameter as a function of effective radius for each condensation. The condensation mass grows rapidly with radius, with a profile similar to one expected for a density distribution of $\rho \propto r^{-1.5}$ (dotted line in **a**) until it is close to the condensation boundary. In comparison, the dashed line shows the expected result in hydrostatic equilibrium ($\rho \propto r^{-2}$), which is

different to the observed distribution. The virial parameter decreases with radius until it reaches a minimum of ~ 1.5 , and then it slowly increases until it reaches the condensation boundary. Notice that virial parameters below the horizontal line ($\alpha = 2$) imply bound condensations. The grey shaded region marks the regime where the effective radius is smaller than the angular resolution of the observations. The circles show the values at the half-mass radius.

Extended Data Table 1 | Condensation and protostar parameters

Source	RA	Dec	V_{lsr}	F_{NH_3}	F_{450}
	(hh:mm:ss.sss)	(dd:mm:ss.ss)	(km s^{-1})	(Jy km s^{-1})	(Jy)
B5-IRS1	03:47:41.548	32:51:43.57	10.21 ± 0.04	—	—
B5-Cond1	03:47:38.928	32:52:15.31	10.43 ± 0.03	0.349 ± 0.001	0.992 ± 0.009
B5-Cond2	03:47:41.627	32:51:56.81	10.23 ± 0.01	0.251 ± 0.001	—
B5-Cond3	03:47:42.778	32:51:30.31	10.30 ± 0.01	0.285 ± 0.001	—

RA, right ascension; Dec., declination; V_{lsr} , central velocity of the observed molecular line; F_{NH_3} , flux measured in the $\text{NH}_3(1,1)$ integrated intensity map; F_{450} , flux measured in the SCUBA-2 450 μm map.